Investigation of Oxide Inclusions and Primary Carbonitrides in Inconel 718 Superalloy Refined through Electroslag Remelting Process

XI-CHUN CHEN, CHENG-BIN SHI, HAN-JIE GUO, FEI WANG, HAO REN, and DI FENG

The effect of remelting atmosphere and calcium treatment during electroslag remelting (ESR) of Inconel 718 superalloy on the oxide inclusions and primary carbonitrides was investigated. The results show that after ESR refining combined with calcium treatment, the original oxide inclusions in the electrode, mainly $MgO{\cdot}Al_2O_3$ spinels and some MgO inclusions, were modified to $CaO\text{-}Al_2O_3$ system inclusions or the inclusions of $MgO{\cdot}Al_2O_3$ spinel core surrounded by $CaO\text{-}MgO\text{-}Al_2O_3$ system inclusion layer. Without the calcium treatment in ESR process, all the oxide inclusions in superalloy ingots are $MgO{\cdot}Al_2O_3$ spinels. All the oxide inclusions in ESR ingots act as the nucleation site for carbonitride (Nb,Ti)CN with two-layer structure precipitation, except for those with a single (Nb,Ti)CN layer containing a small amount of Ti and N in the ingot refined by a proper amount of calcium addition in ESR process. The carbonitrides (Nb,Ti)CN formed directly on the oxide inclusion have a small amount of Nb and C as well as a relatively fixed atomic ratio of Nb/Ti (about 0.6:1). There is a Nb-rich and C-rich (Nb,Ti)CN layer on the pre-existing (Nb,Ti)CN formed on the oxide inclusion. The size of the observed carbonitrides is in the range of 5 μm to 15 μm. The calcium treatment in the ESR process has a significant effect on the morphology of carbonitrides in superalloy ingot due to modification of oxide inclusions by Ca-treatment resulting in the change of precipitation and growth conditions for carbonitrides. The morphologies of carbonitrides were changed from clustered block or single octahedral to skeleton-like after calcium treatment.

DOI: 10.1007/s11663-012-9723-6

I. INTRODUCTION

PRIMARY MC carbide is a type of the common precipitates in superalloys.[1,2] Sometimes oxide inclusions precipitation is also inevitable in some superalloys.[3,4] In addition, oxide bifilms are normally created during casting of nickel-base superalloys.[5] These precipitates have an important effect on the mechanical properties, solidification behavior, cracks occurrence, and fatigue life of nickel-base superalloys.[5–10] Oxide inclusions normally tend to act as the nucleation site for other precipitates, which form during cooling and/or solidification, such as carbides[11,12] and sulfides.[13] The oxide bifilms can also act as substrates for carbide precipitation in nickel-base superalloy,[10] and they act as preferred substrates for some intermetallics nucleation and growth in aluminum alloy.[14–16] The removal of oxide inclusions and oxide bifilms from superalloy and alloy melts is one of the main development efforts in the superalloy and alloy production. It is quite necessary, but difficult, to completely remove these precipitates in superalloy and alloy melts. With a lower melting temperature of oxide inclusion, the deformability of the inclusion would be improved.[17] Therefore, modification of some oxide inclusions to the low-melting-point oxide inclusions is an effective way to lower their detriment to final products. Calcium treatment is generally used for modification of $MgO{\cdot}Al_2O_3$ or Al_2O_3 inclusions to calcium aluminates with low melting point in steelmaking process to improve final product performance.[18–20]

It is expected that calcium treatment will be beneficial to minimize the nucleation sites for carbides and their detriment to subsequent deformation process, provided that similar modification is realized during electroslag remelting (ESR) of superalloy. However, there is no report on whether $MgO{\cdot}Al_2O_3$ inclusions can be modified to calcium aluminates with low melting point by calcium treatment during ESR of steel or nickel-base superalloy. The formation and modification of oxide inclusions in nickel-base superalloy during superalloy production processes are expected to be different from that in steelmaking process, due to high alloying element content in nickel-base superalloy and big differences in production technology.

Xi-CHUN CHEN, Senior Engineer, HAO REN, Engineer, and DI FENG, Professor, are with the Research Institute of High Temperature Materials, Central Iron and Steel Research Institute (CISRI), Beijing 100081, P.R. China. CHENG-BIN SHI and FEI WANG, Ph.D. Candidates, and HAN-JIE GUO, Professor, are with the State Key Laboratory of Advanced Metallurgy and with School of Metallurgical and Ecological Engineering, University of Science and Technology Beijing (USTB), Beijing 100083, P. R. China. Contact e-mail: shicb09@hotmail.com

Manuscript submitted April 30, 2012.
Article published online September 21, 2012.

Extensive studies have been focused on controlling solidification structure and microstructure of Inconel 718 superalloy.[21–24] However, few studies regarding the characteristics and control of oxide inclusions in nickel-base superalloy have been done. In the current work, the characteristics of oxide inclusions and primary carbonitrides in Inconel 718 superalloy produced by laboratory-scale ESR unit were examined by (I) two-dimensional determination on a polished cross section of metal sample and (II) three-dimensional investigation of precipitates electrolytically extracted from metal sample together with scanning electron microscopy (SEM) equipped with energy dispersive X-ray spectroscopy (EDS) analysis. The effect of calcium treatment on modification of the oxide inclusions and primary carbonitrides was investigated. The evolution mechanism of oxide inclusions during ESR of Inconel 718 was proposed on the basis of laboratory experimental results and thermodynamic analysis.

II. EXPERIMENTAL

A. *Experimental Procedure*

Superalloy electrode materials were produced in an MgO crucible of a vacuum-induction melting (VIM) furnace. After vacuum-induction melting, the liquid superalloy was cast into the ingots of 105 mm in diameter, which were thereafter used as consumable electrodes in ESR experiments. The chemical composition of the produced consumable electrode is given in Table I.

The schematic diagram of laboratory-scale ESR unit is shown in Figure 1. The inner diameter of water-cooled copper mold is 170 mm. Four heats were conducted under different remelting conditions in this ESR furnace at the Central Iron and Steel Research Institute. The operating alternating current (AC) current and voltage were maintained at about 1800 A and 49 V, respectively. The outlet temperature of the mold cooling water was maintained at about 298 K (25 °C). The liquid slag starting technique was employed in each heat. The individual remelting condition in each ESR experiment is summarized as follows:

- Exp. No. T1: Remelting under atmosphere, without calcium treatment
- Exp. No. T2: Remelting under Ar gas atmosphere (Ar gas flow rate of 50 NL/min), without calcium treatment
- Exp. No. T3: Remelting under Ar gas atmosphere (Ar gas flow rate of 50 NL/min) combined with calcium treatment
- Exp. No. T4: Remelting under Ar gas atmosphere (Ar gas flow rate of 50 NL/min) combined with calcium treatment

In the case of calcium treatment, the mixture of 40 mass pct calcium powder, 40 mass pct iron powder, and 20 mass pct CAF60 slag was continually added into the slag pool. The detailed descriptions of the addition technique were given in the authors' previous publication.[25] The Ca-containing mixture addition rate was about 35 kg/t in experiment T3 and about 8.8 kg/t in experiment T4. Premelted slag CAF60 (60 mass pct CaF_2, 20 mass pct CaO, and 20 mass pct Al_2O_3) was used in each ESR experiment. The premelted slag was calcined at 773 K (500 °C) for at least 6 hours to remove moisture before ESR experiments. The superalloy ESR ingots produced in experiment T1, experiment T2, experiment T3, and experiment T4 were designated as ESR-1, ESR-2, ESR-3, and ESR-4, respectively.

B. *Chemical Analysis and Microscopic Observation*

The contents of soluble aluminum, magnesium, and calcium in superalloy samples were determined by the inductively coupled plasma-mass spectroscopy. The oxygen and nitrogen contents in each ESR ingot were determined by the inert gas fusion-infrared absorptiometry and inert gas fusion–thermal conductivity method, respectively. The analyzed results are given in Table II.

The metal samples of 15 mm × 15 mm × 15 mm that were cut from the electrode and superalloy ingots (designated as samples E0, E1, E2, E3, and E4, respectively) were polished by SiC papers and diamond paste in order to analyze the characteristics of precipitates by SEM

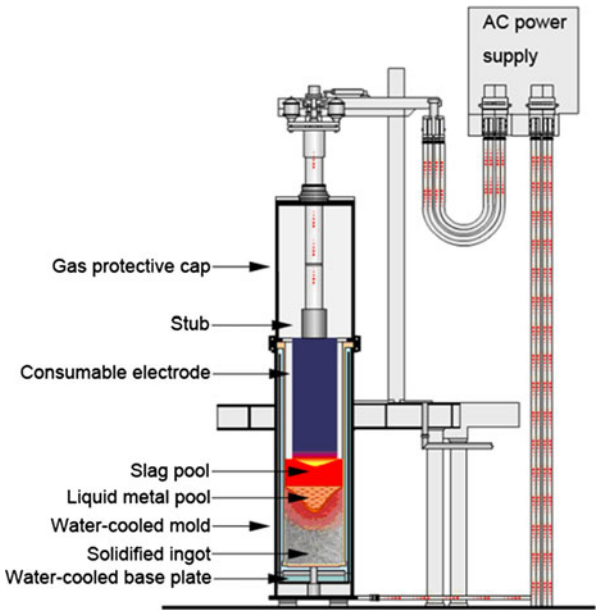

Fig. 1—Schematic diagram of experimental apparatus.

Table I. Chemical Composition of Consumable Electrode Used in Each Heat (mass pct)

C	Si	Mn	P	Cr	Cu	Mo	Al	Fe	Nb	Ti	B	Mg	Ca	O	N	Ni
0.078	0.05	0.0027	0.0036	18.7	0.003	3.1	0.71	18.5	5.16	1.09	0.0025	0.0034	< 0.0005	0.0007	0.0038	52.53

Table II. Magnesium, Calcium, and Aluminum Contents in ESR Ingots (mass pct)

Exp. No.	Sample No.	O	N	Mg	Ca	Sol. Al
T1	E1	0.0010	0.0046	0.0014	< 0.0005	0.55
T2	E2	0.0016	0.0050	0.0009	< 0.0005	0.80
T3	E3	0.0024	0.0064	0.0005	0.0045	0.82
T4	E4	0.0008	0.0041	0.0011	0.0010	0.68

(FEI Quanta-600; FEI Corporation, Hillsboro, OR) equipped with EDS (EDAX Genesis-7000; EDAX Inc., Mahwah, NJ) for the direct observation on well-polished surface. About 50 inclusions in each sample were randomly selected to examine the microstructure, size, and chemical compositions with SEM-EDS. In addition, SEM and electron probe microanalyzer (EPMA; JXA-8100; JEOL Ltd., Tokyo, Japan) were employed to further analyze the element mappings of precipitated particles.

The electrolytic extraction technique was employed to extract the precipitates in superalloy ingots. The superalloy sample of 12 mm in diameter and 100 mm in length, which was cut from superalloy ingots, was electrolyzed in organic solution under anode current density of no greater than 100 mA/cm^2. After dissolution of the metal matrix, the non-dissolved precipitates were elutriated with ethanol and then collected on a thin copper foil. The extracted particles were then examined by SEM-EDS. In addition, some of the precipitates that were extracted from superalloy samples by electrolytic extraction technique were prepared for determination of the cross sections of these precipitates by SEM-EDS. A thin copper foil inlaid with the extracted precipitates was embedded into epoxy resin. Thereafter, this sample was polished by SiC papers. Finally, a gold film was sprayed onto the surface of the extracted precipitates before SEM-EDS analysis. A detailed description of this technique is available in the previous publication.[13]

III. RESULTS AND DISCUSSION

A. *Characteristics of Oxide Inclusions and Primary Carbonitrides in Inconel 718 ESR Ingots*

The cross section of each metal sample that was cut from the electrode and ESR ingots was examined by SEM-EDS. Figure 2 shows the SEM images and EDS analysis results of typical inclusions in the consumable electrode and ESR ingots. It is clear from Figure 2 that a three-layer structure can be distinguished in all these precipitates by their color. The SEM images and EDS analysis results of typical inclusions observed in sample E0 that was cut from the electrode material are shown in Figures 2(a) through (c). It appears from Figures 2(a) through (c) that oxide inclusion acts as the nucleation core of carbonitride (Nb,Ti)CN, which would also act as the subsequent nucleation site for outermost carbonitride (Nb,Ti)CN precipitation. The SEM-EDS analysis shows that the compositions of the carbonitrides (Nb,Ti)CN formed on oxide inclusions are different from that of the outermost carbonitrides (Nb,Ti)CN. The difference would be discussed later based on further examination and theoretical analysis. The oxide inclusions in the electrode are mainly $MgO{\cdot}Al_2O_3$ spinels and a few pure MgO inclusions.

The typical inclusions observed in sample E1 are shown in Figures 2(d) through (f). The inclusions display a complex structure in the form of $MgO{\cdot}Al_2O_3$ spinel cores surrounded by outer carbonitrides (Nb,Ti)CN and outermost carbonitrides (Nb,Ti)CN layer. $MgO{\cdot}Al_2O_3$ spinel is the only oxide inclusion found in sample E1. Figures 2(g) through (i) show the SEM images and EDS analysis results of typical inclusions in the ingot produced in experiment T2. All the precipitates observed by SEM-EDS in sample E2 are complex precipitates composed of $MgO{\cdot}Al_2O_3$ spinel core surrounded by outer carbonitrides (Nb,Ti)CN and outermost carbonitrides (Nb,Ti)CN layer. All the observed oxide inclusions in sample E2 are $MgO{\cdot}Al_2O_3$ spinels. It should be pointed out that, not only in sample E1 but also in sample E2, the compositions of the outermost carbonitrides (Nb,Ti)CN are different from that formed on oxide inclusions.

Figures 2(j) through (l) represent the SEM images and EDS analysis results of typical inclusions in sample E3. The oxide inclusions are mainly CaO and a few CaO-Al_2O_3 system inclusions. These oxide inclusions act as the nucleation sites for outer carbonitrides and outermost carbonitrides (Nb,Ti)CN precipitation. The morphology and EDS analysis results of precipitates observed in sample E4 are shown in Figures 2(m) through (p). All the inclusions observed by SEM-EDS in sample E4 are complex precipitates, which are composed of oxide inclusion that acts as a core and an outer carbonitride layer with a small amount of Ti and N. All the oxide inclusions were identified as $MgO{\cdot}Al_2O_3$ spinel core surrounded by an outer CaO-MgO-Al_2O_3 layer. It can be seen that these complex oxide inclusions are spherical in shape. This observation indicates that the irregular oxide inclusions can be changed into the spherical after proper calcium treatment. No inclusion of MgO core surrounded by an outer carbonitride layer was found in ESR-1, ESR-2, ESR-3, or ESR-4.

Figure 3 represents SEM-mappings of a typical complex inclusion in sample E2 determined by SEM-EPMA. It can be seen from SEM-EPMA analysis result that the inclusion has concentrated Mg, Al, and O in the core, and an outer Ti-rich and N-rich layer as well. In the outermost layer, the Nb and C concentrations are high. It can also be seen that there is a fuzzy hierarchy between each layer. The region concentrated with Nb and C also contains a small amount of Ti and N. Meanwhile, a small amount of Nb and C exists in the region concentrated with Ti and N (*i.e.*, the layer

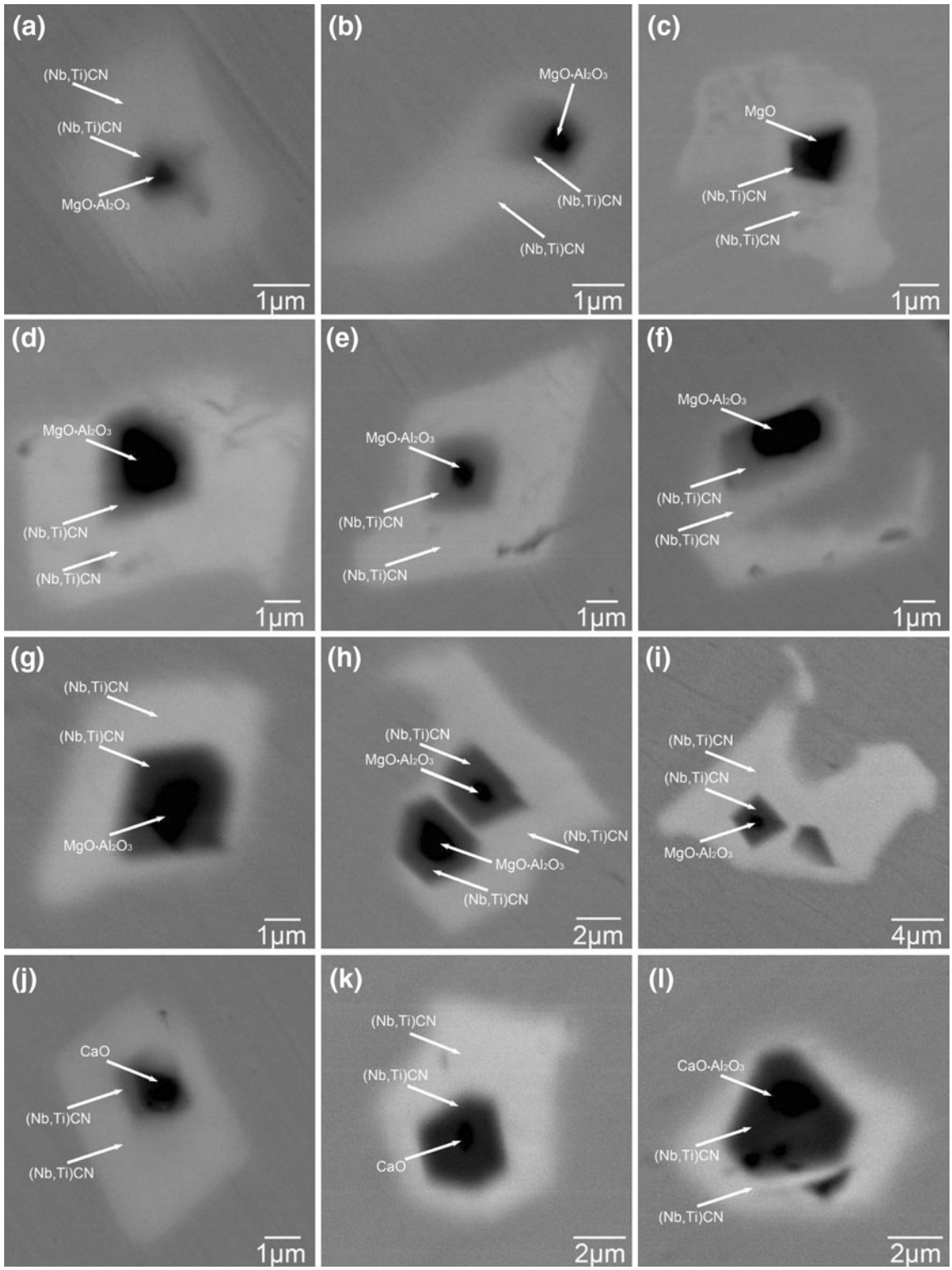

Fig. 2—SEM images and EDS analysis results of typical inclusions observed in consumable electrode and each ESR ingot: (*a*)–(*c*) sample E0, (*d*)–(*f*) sample E1, (*g*)–(*i*) sample E2, (*j*)–(*l*) sample E3, and (*m*)–(*p*) sample E4.

surrounding on oxide inclusion core). It is considered to be the result of subsequent atom interdiffusion at the interface between the two layers during the complex inclusion formation. The core of the complex inclusion was identified as $MgO{\cdot}Al_2O_3$ spinel. Carbonitride formed on oxide inclusion was (Nb,Ti)CN with a small amount of Nb and C as confirmed by SEM-EDS and further supported by SEM-EPMA. It is also revealed by SEM-EDS together with SEM-EPMA that the outermost carbonitride (Nb,Ti)CN contains a small amount of Ti and N. The detailed discussion on carbonitride compositions will be presented later.

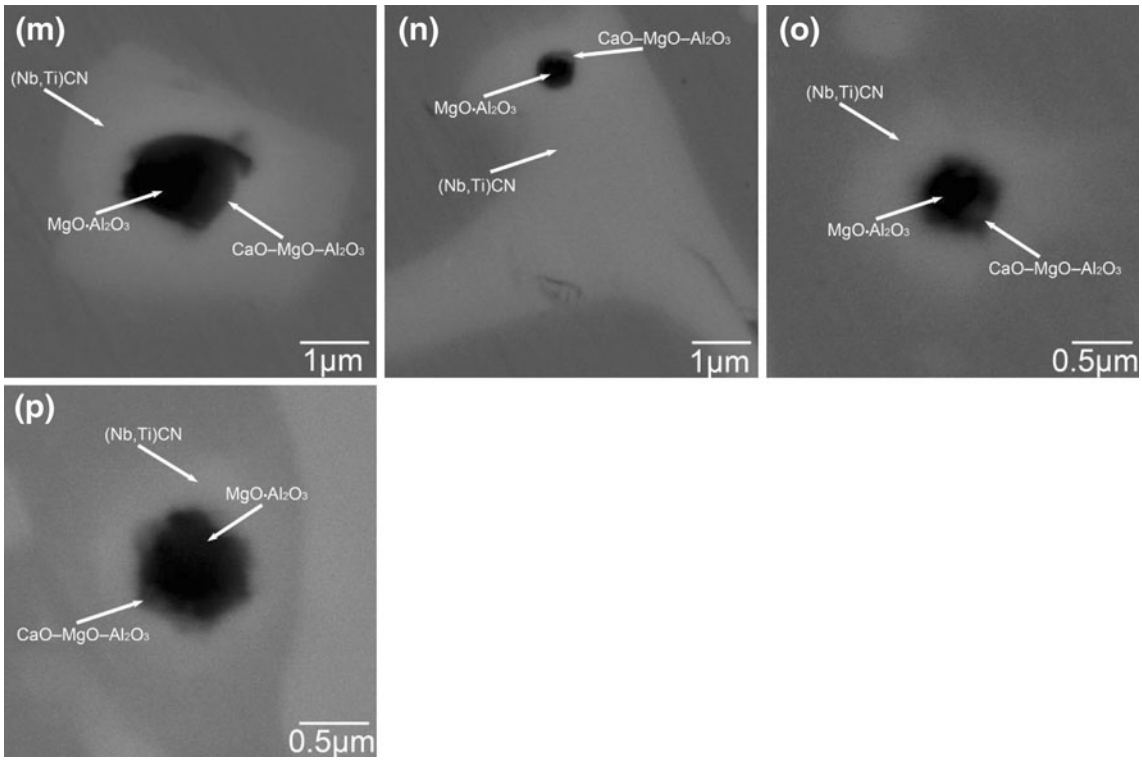

Fig. 2—Continued.

In order to determine the three-dimensional morphology and actual size of precipitates in ESR ingots, and to exclude the metal matrix effect on analysis of inclusion compositions, an electrolytic extraction technique in combination with SEM-EDS analysis were employed. Figure 4 shows the SEM images of extracted precipitates observed in each superalloy ESR ingot. It was confirmed by SEM-EDS determination that all the extracted particles in samples E1, E2, E3, and E4 were (Nb,Ti)CN particles containing a small amount of Ti and N. It is clear from Figures 4(a) through (d) that most of the carbonitrides have a large size (in the range of 5 μm to 15 μm). As can be seen, all of these extracted carbonitrides have obvious cone angles. The morphologies of the observed carbonitrides in superalloy ingots produced with and without calcium addition in ESR process are different. The carbonitrides in the superalloy ingots (*i.e.*, ESR-1 and ESR-2) produced without calcium addition are clustered block or single octahedral form. In the case of superalloy ingots produced with calcium treatment, the morphology of the observed carbonitrides in ESR-3 and ESR-4 is in skeleton-like form.

Figure 5 represents the three-dimensional SEM images and EDS analysis results of the individual precipitates extracted from ESR ingots. All of these inclusions extracted from different ESR ingots were identified as (Nb,Ti)CN containing a small amount of Ti and N. It was confirmed by SEM-EDS that the atomic ratios of Nb, Ti, C, and N slightly varied in different carbonitrides. It should be pointed out, however, that all the observed three-dimensional carbonitrides have much higher atomic percent of Nb than that of Ti. The atomic ratios of Nb/Ti for different carbonitrides are in a narrow range from 6:1 to 9:1.

By comparing the results from the direct observation on a well-polished surface by SEM-EDS and the determination of three-dimensional extracted inclusions, it cannot be concluded from the above SEM-EDS results shown in Figure 5 that whether the observed three-dimensional inclusions are pure (Nb,Ti)CN or the complex inclusions in the form of an oxide core surrounded by outer (Nb,Ti)CN layer. Therefore, the cross sections of the extracted particles were examined by SEM-EDS. Figure 6 shows SEM images and EDS analysis results of the cross sections of the extracted precipitates from ESR-1 and ESR-3. It can be seen that the extracted inclusions are a three-layer structure. Oxide inclusion acts as the nucleation core for outer (Nb,Ti)CN layer. Meanwhile, there is a (Nb,Ti)CN layer with a small amount of Ti and N surrounding on interlayer (Nb,Ti)CN. All the oxide inclusion cores in the extracted inclusions in ESR-1 are $MgO{\cdot}Al_2O_3$ spinels. The oxide inclusions in ESR-3 are mainly CaO, and a few $CaO\text{-}Al_2O_3$ system inclusions were occasionally observed. Because the C and N contents in precipitates cannot be quantitatively determined by SEM-EDS, the analysis of carbonitride compositions was only focused on the concentration of Nb and Ti in carbonitrides. The atomic ratio of Nb/Ti in most of the outer (Nb,Ti)CN layer is about 7.5:1. While this ratio in the inner (Nb,Ti)CN layer, which directly formed on oxide inclusion, is about 0.6:1. The outermost (Nb,Ti)CN layer has higher atomic percentage of Nb than that of Ti. But the inner (Nb,Ti)CN layer has higher atomic percentage of Ti than that of Nb. This

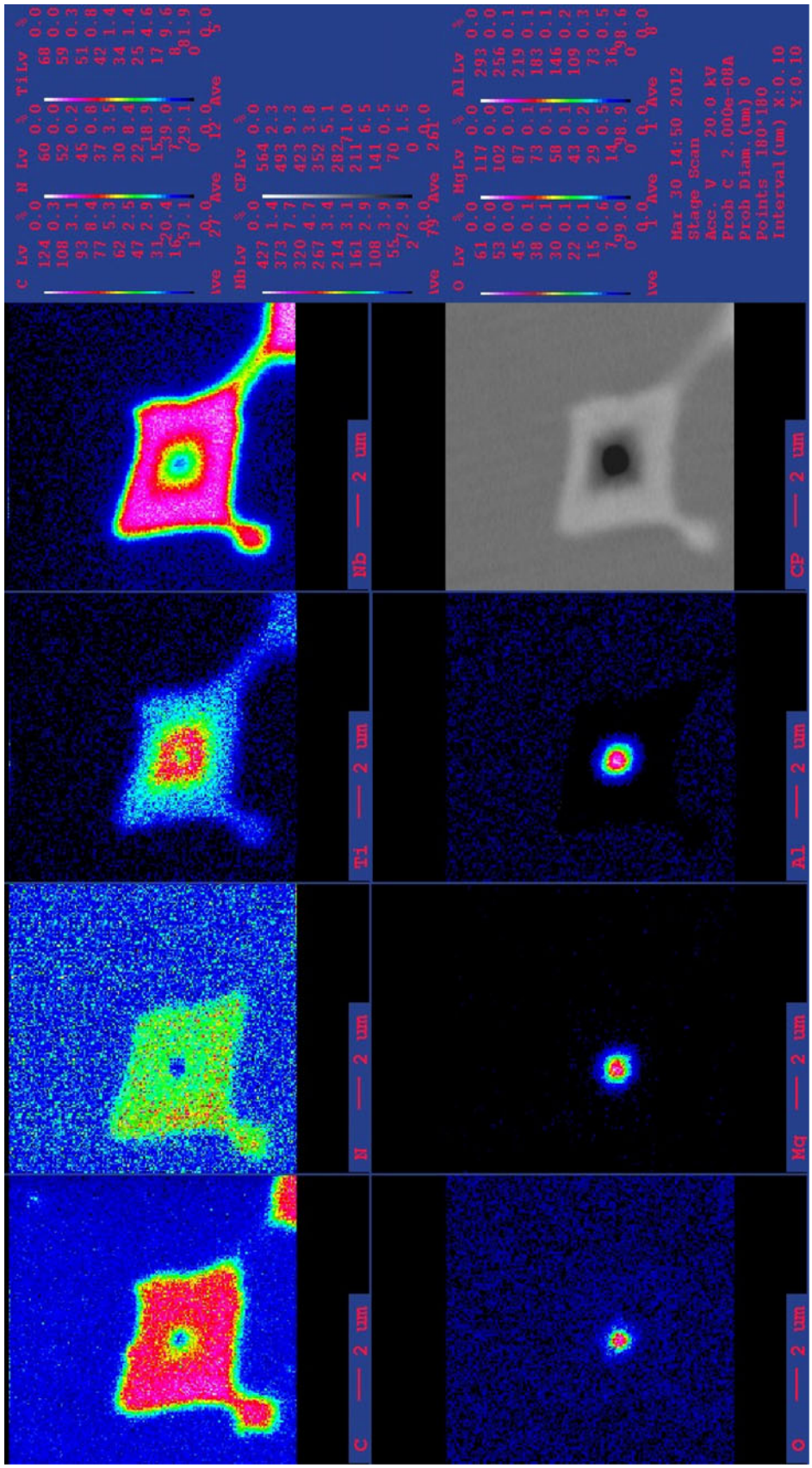

Fig. 3—SEM-mappings of a typical complex inclusion in sample E2 revealed by SEM-EPMA.

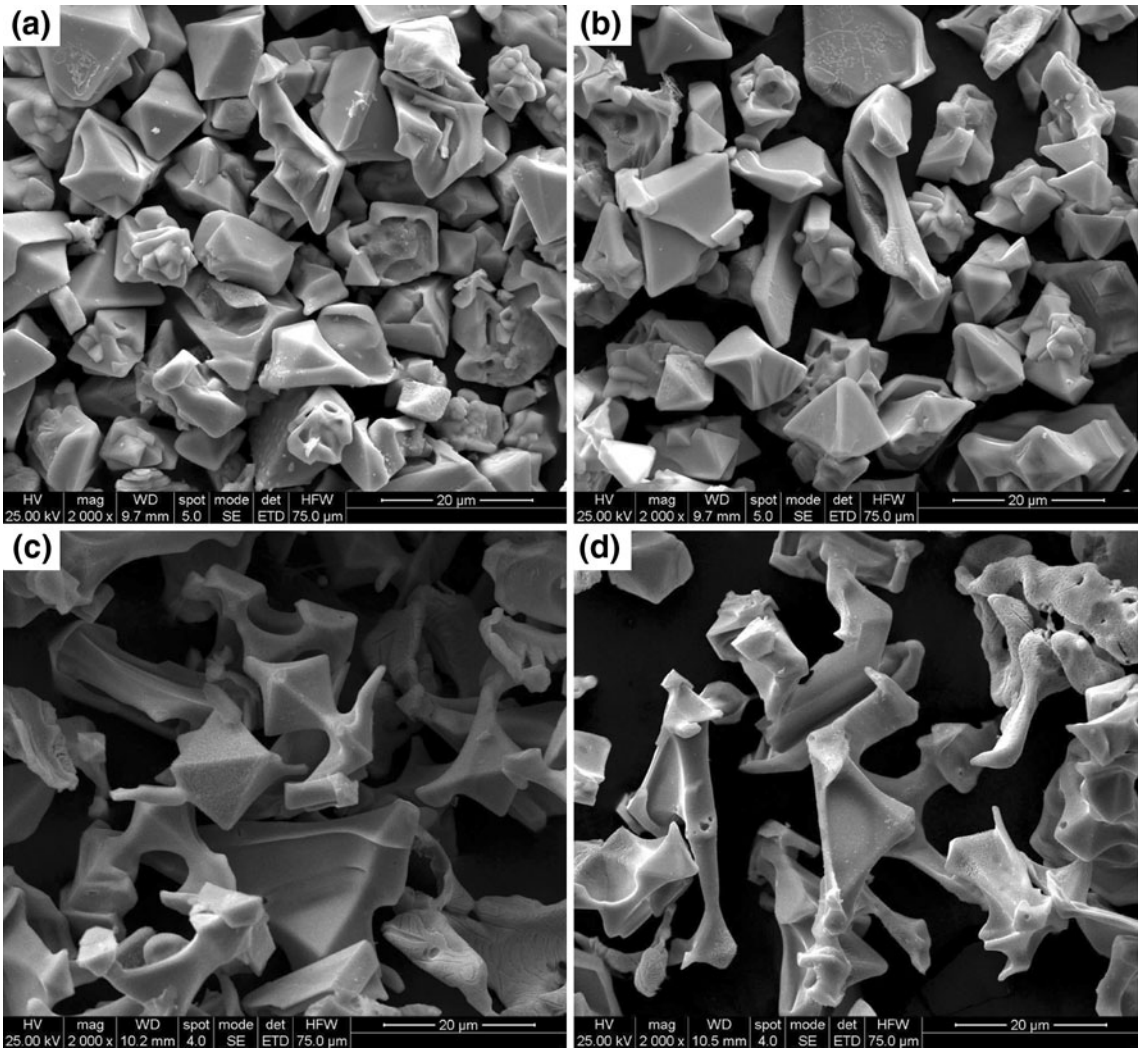

Fig. 4—SEM images of the extracted carbonitrides (Nb,Ti)CN observed in each ESR ingot: (*a*) ESR-1, (*b*) ESR-2, (*c*) ESR-3, and (*d*) ESR-4.

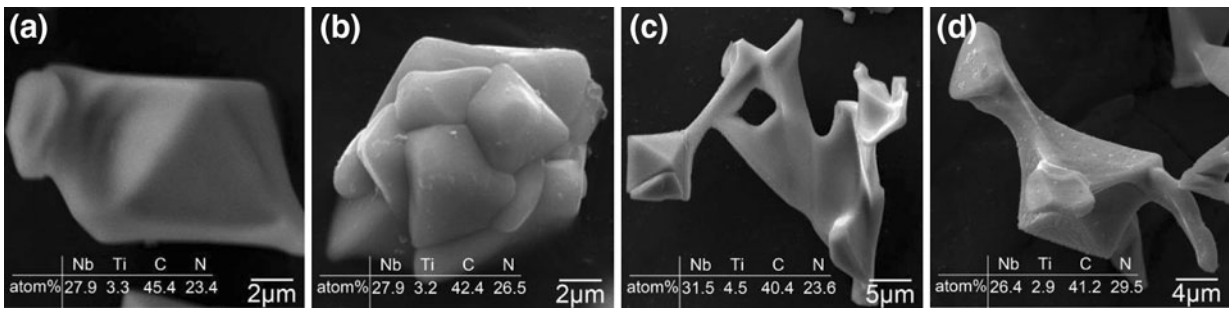

Fig. 5—Three-dimensional SEM images and EDS analysis results of typical precipitates observed in each ESR ingot: (*a*) sample E1, (*b*) sample E2, (*c*) sample E3, and (*d*) sample E4.

result is consistent with the observation by two-dimensional determination shown in Figure 2.

It can also be seen by comparing the direct observation of well-polished surface with SEM-EDS and the determination of three-dimensional extracted inclusions that the actual size and morphology of the observed inclusions can hardly be represented by the direct observation of well-polished surface with SEM-EDS, *i.e.*, the two-dimensional determination. Figure 7 shows schematic view of the randomly selected cross-sectional plane for direct two-dimensional observation by SEM-EDS. The cross-sectional plane A and cross-sectional plane B denote the randomly chosen cross-sectional plane for the direct two-dimensional observation. It can

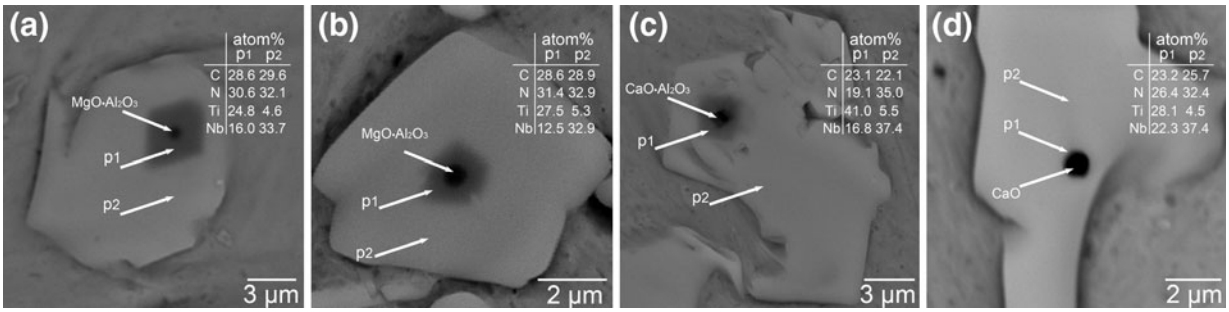

Fig. 6—SEM images and EDS analysis results of the cross section of typical extracted inclusions in ESR ingots: (*a*) and (*b*) in ESR-1, (*c*) and (*d*) in ESR-3.

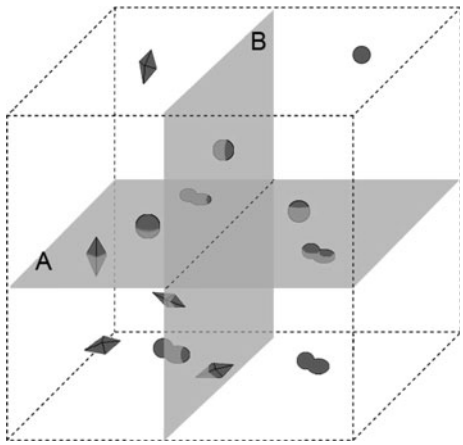

Fig. 7—Schematic view of the possibly selected cross-sectional plane for direct two-dimensional observation by SEM-EDS.

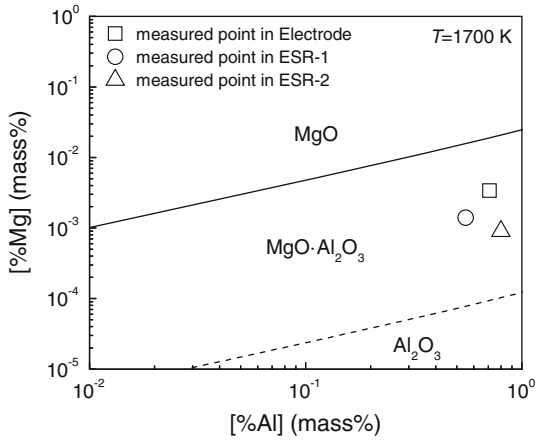

Fig. 8—Phase stability diagram of $MgO/MgO{\cdot}Al_2O_3/Al_2O_3$ inclusions in nickel-base superalloy.

be seen that the observed size and morphology of the observed inclusions are obviously different when different cross-sectional planes were used for direct observation on polished surface. Therefore, it is not very meaningful to discuss the morphology of the observed inclusions under the condition of two-dimensional analysis (*i.e.*, the direct observation on the polished cross section of metal sample with SEM-EDS). No detailed description of the morphology of the observed inclusions was presented. It is because the morphology of inclusions (especially large inclusions) under the condition of the direct observation on the polished cross section of metal sample is strongly dependent on the axis and direction of cutting during sample preparation. It should be noted that, although different cross-sectional planes were chosen to obtain the polished surface for direct SEM-EDS observation, the composition of the same inclusion is identical.

B. *Evolution of Oxide Inclusions During ESR Process*

Vacuum-induction melting is an indispensable step in Inconel 718 superalloy production. Thereafter, the produced ingot is used as consumable electrode in ESR production. The presence of oxide inclusions, such as MgO and $MgO{\cdot}Al_2O_3$ spinel, which have a high melting point and are non-deformable, in the electrode may be inevitable, which can directly or indirectly originate from refractory materials of VIM furnace in the production of the electrode materials. It is quite necessary, but hardly feasible, to completely remove these oxide inclusions. A complementary method is to modify the high-melting-point inclusions to low-melting-point inclusions such as liquid calcium aluminate.

The liquid metal film temperature at the electrode tip is close to the liquidus temperature of the electrode materials in the ESR process.[26] Hence, it is assumed that the temperature of the liquid metal film at electrode tip in the current experiments is equal to the liquidus temperature of the studied Inconel 718 superalloy, *i.e.*, 1613 K (1340 °C).[27] The temperature of slag pool is overheated in ESR process, and it is higher than that in liquid metal pool.[28,29] It is known that the precipitation of primary MC carbides and TiN in nickel-base superalloy occurs below the freezing point temperature of the superalloy material in residual liquid superalloy during liquid superalloy solidification.[9,30–33] There are no reports that solid carbide particles exist in liquid phase in this superalloy or that any particles remain undissolved during this superalloy melting. With the high temperature at the electrode tip and in slag pool during electroslag remelting of Inconel 718 superalloy, carbonitrides in the electrode would dissociate into [Nb], [Ti], [C], and [N] in liquid metal film during liquid metal film

formation at electrode tip. Thereafter, oxide inclusions were exposed to liquid metal. The similar result showing that carbides in Ni-base superalloy melt back into the liquid superalloy was also reported by other researchers.[9,34] During liquid metal solidification at the bottom of liquid metal pool in water-cooled mold, oxide inclusions would act as the nucleation sites for carbonitrides precipitation. In the current study, the thermodynamic analysis was focused on the evolution of oxide inclusions during ESR process.

The stability diagram including the phase boundaries among MgO, $MgO{\cdot}Al_2O_3$ and Al_2O_3 was developed, as shown in Figure 8, based on consideration of the following chemical reactions

For $MgO/MgO{\cdot}Al_2O_3$ boundary

$$2[Al] + 4MgO(s) = 3[Mg] + MgO \cdot Al_2O_3(s) \qquad \Delta G_1^o = 834,928 - 360.432T \quad (J/mol) \qquad [1]$$

The equilibrium constant of reaction [1] can be expressed as

$$K_1 = \frac{a_{MgO{\cdot}Al_2O_3} \cdot a_{Mg}^3}{a_{MgO}^4 \cdot a_{Al}^2} = \frac{a_{MgO{\cdot}Al_2O_3} \cdot f_{Mg}^3[pct\ Mg]^3}{a_{MgO}^4 \cdot f_{Al}^2[pct\ Al]^2} \qquad [2]$$

where f_{Mg} and f_{Al} are the activity coefficient of magnesium and aluminum in liquid superalloy, respectively, and it can be expressed by the following formula

$$\lg f_i = \sum (e_i^j[pct\ j] + r_i^j[pct\ j]^2) \qquad [3]$$

where e_i^j and r_i^j are the first-order and second-order interaction parameters, respectively. The available first-order and second-order interaction parameters in liquid nickel used in the current study are summarized as follows: $e_{Mg}^{Ni} = -0.026$,[35] $e_{Mg}^{Cr} = 0.01$,[36] $e_{Al}^{Al} = 0.08$,[35] $e_{Al}^{Ni} = -0.029$,[36] $e_{Al}^{Cr} = 0.0096$,[35] $e_{Al}^{N} = -0.004$,[35] $r_{Al}^{Al} = -0.0006$,[35] $r_{Al}^{Ni} = 0.000164$.[37] Strictly speaking, more second-order interaction parameters and cross-product terms are needed to precisely calculate the activity coefficient of f_{Mg} and f_{Al}. However, these parameters are assumed as zero in the current work due to the lack of these thermodynamic data reported in the literature.

The standard Gibbs free energy change for reaction [1] ΔG_1^o was obtained by the combination of standard Gibbs free energy change for reactions [4] through [6]

$$2[Al] + 3[O] = Al_2O_3(s) \qquad \Delta G_4^o = -1,157,000 + 356.2T^{[35]} \quad (J/mol) \qquad [4]$$

$$[Mg] + [O] = MgO(s) \qquad \Delta G_5^o = -670,906 + 233.644T^{[35,38]} \quad (J/mol) \qquad [5]$$

$$MgO(s) + Al_2O_3(s) = MgO \cdot Al_2O_3(s) \qquad \Delta G_6^o = -20,790 - 15.7T^{[39]} \quad (J/mol) \qquad [6]$$

For $MgO{\cdot}Al_2O_3/Al_2O_3$ boundary

$$3[Mg] + 4Al_2O_3(s) = 2[Al] + 3MgO \cdot Al_2O_3(s) \qquad \Delta G_7^o = -918,088 + 297.632T \ (J/mol) \qquad [7]$$

The equilibrium constant of reaction [7] can be expressed as

$$K_7 = \frac{a_{MgO{\cdot}Al_2O_3}^3 \cdot a_{Al}^2}{a_{Al_2O_3}^4 \cdot a_{Mg}^3} = \frac{a_{MgO{\cdot}Al_2O_3}^3 \cdot f_{Al}^2[pct\ Al]^2}{a_{Al_2O_3}^4 \cdot f_{Mg}^3[pct\ Mg]^3} \qquad [8]$$

The standard Gibbs free energy change for reaction [7] ΔG_7^o was also obtained by the combination of standard Gibbs free energy change for reactions [4] through [6].

It is not possible in the operation to measure the temperature in liquid metal pool under the present experimental conditions. Considering that the liquidus temperature of Inconel 718 superalloy is 1613 K (1340 °C), 1700 K (1427 °C) was used as the temperature of liquid metal pool during electroslag remelting of the superalloy in the present thermodynamic analysis. It should be pointed out that the activities of MgO and $MgO{\cdot}Al_2O_3$ were taken as unity[39,40] and 0.8[39,40] for calculation of $MgO/MgO{\cdot}Al_2O_3$ boundary using Eq. [2], respectively, due to the negligibly small solubility of Al_2O_3 in MgO. The activities of Al_2O_3 and $MgO{\cdot}Al_2O_3$ were taken as unity[39,40] and 0.47[39,40] for calculation of $MgO{\cdot}Al_2O_3/Al_2O_3$ boundary using Eq. [8], respectively, due to the negligibly small solubility of MgO in Al_2O_3.

It can be seen from Figure 8 that the contents of Mg and Al in the electrode, ESR-1, and ESR-2 are in the region of $MgO{\cdot}Al_2O_3$ spinels formation. The thermodynamic analysis suggests the formation of $MgO{\cdot}Al_2O_3$ spinels in the electrode, ESR-1, and ESR-2. The result is consistent with the experimental determination in the electrode, ESR-1, and ESR-2 by SEM-EDS.

It can be found from the experimental results and the above thermodynamic analysis that $MgO{\cdot}Al_2O_3$ spinels and MgO inclusions are the only oxide inclusions in the electrode. It is considered that MgO inclusions in the electrode originate from refractory material due to the dissolution of MgO crucible material of vacuum-induction melting furnace according to the following reaction:

$$MgO(s)_{in\ refractory} = MgO(s) \qquad [9]$$

Meanwhile, dissolved aluminum in liquid superalloy [Al] would react with MgO originating from refractory material forming $MgO{\cdot}Al_2O_3$ spinels during vacuum induction melting, as expressed by following reaction:8

$$4MgO + 2[Al] = MgO \cdot Al_2O_3(s) + 3[Mg] \qquad [10]$$

It is just for simplicity in this paper that the $MgO{\cdot}Al_2O_3$ spinels are written as stoichiometric $MgO{\cdot}Al_2O_3$. In fact, $MgO{\cdot}Al_2O_3$ spinels are solid solutions between $MgAl_2O_4$ and Al_2O_3,[19] rather than stoichiometric compound.

All the oxide inclusions in samples E1 and E2 are $MgO{\cdot}Al_2O_3$ spinels. This could be due to the fact that the remaining original MgO inclusions originating from the electrode react with dissolved aluminum in liquid metal pool, according to Eq. [1], to form $MgO{\cdot}Al_2O_3$ spinels. In addition, some $MgO{\cdot}Al_2O_3$ spinels remaining in samples E1 and E2 may be the original $MgO{\cdot}Al_2O_3$ spinels in the electrode, which have not been removed during ESR process. It is not possible to determine whether the remaining $MgO{\cdot}Al_2O_3$ inclusions in samples E1 and E2 are the original $MgO{\cdot}Al_2O_3$ spinels or the newly precipitated $MgO{\cdot}Al_2O_3$ spinels in liquid metal pool.

In the case of calcium addition (Exp. No. T4), the newly formed $MgO{\cdot}Al_2O_3$ spinels according to Eq. [1] and the original $MgO{\cdot}Al_2O_3$ spinels remaining in liquid metal phase react with dissolved calcium as expressed by the following reaction:

$$[\mathrm{Ca}] + (x + 1/y)(y\mathrm{MgO} \cdot \mathrm{Al_2O_3})(\mathrm{s}) = (\mathrm{CaO} \cdot xy\mathrm{MgO} \cdot (x + 1/y)\mathrm{Al_2O_3})_{\mathrm{inclusion}} + [\mathrm{Mg}] \quad [11]$$

This is the reason that many $CaO\text{-}MgO\text{-}Al_2O_3$ system inclusions around $MgO{\cdot}Al_2O_3$ spinel cores are found in sample E4. Meanwhile, it has also been confirmed that the modification of $MgO{\cdot}Al_2O_3$ spinels to $CaO\text{-}MgO\text{-}Al_2O_3$ system inclusions can be achieved by calcium treatment during electroslag remelting of superalloy in experiment T4. This is beneficial for improving the plasticity of the inclusions remaining in nickel-base superalloy ESR ingot because many $CaO\text{-}MgO\text{-}Al_2O_3$ system inclusions have low melting points compared with $MgO{\cdot}Al_2O_3$ spinels and MgO inclusions. Many other studies[20,41] have also shown that many oxide inclusions in steel are in the form of $MgO{\cdot}Al_2O_3$ spinel core embedded in $CaO\text{-}MgO\text{-}Al_2O_3$ layer after calcium treatment of $MgO{\cdot}Al_2O_3$ spinels.

However, with an excessive amount of calcium addition, many CaO inclusions (melting point 2845 K [2572 °C]) would form and remain in superalloy ingot, as shown in sample E3. The presence of many CaO inclusions (each of them surrounded by outer (Nb,Ti)CN layer) in ESR-3 is expected to be due to the reaction between excessive dissolved calcium and dissolved oxygen, as shown in Eq. [12].

$$[\mathrm{Ca}] + [\mathrm{O}] = \mathrm{CaO}(\mathrm{s}) \quad [12]$$

The formation of $CaO\text{-}Al_2O_3$ system inclusions found in ESR-3 is expected to be due to the following reaction:

$$[\mathrm{Ca}] + \mathrm{MgO} \cdot x\mathrm{Al_2O_3}(\mathrm{s}) = \mathrm{CaO} \cdot x\mathrm{Al_2O_3}(\mathrm{s}) + [\mathrm{Mg}] \quad [13]$$

Kang *et al.*[20] and Jiang *et al.*[41] showed that $MgO{\cdot}Al_2O_3$ spinels can be changed into $CaO\text{-}MgO\text{-}Al_2O_3$ system inclusions with a very low MgO content or theoretically into $CaO\text{-}Al_2O_3$ system inclusions under the condition of sufficient chemical reaction time and calcium addition. By comparing the oxide inclusions compositions in samples E3 and E4, it is considered that the formation of $CaO\text{-}Al_2O_3$ system inclusions is due to the reduction reaction of MgO component of spinel to [Mg] in liquid metal by sufficient amount of calcium. The similar mechanism was also described in Reference 18.

The pre-existing oxide inclusions in liquid superalloy can act as the nucleation sites for subsequent nitrides precipitation. During the cooling of liquid superalloy from the liquid metal pool temperature to the liquidus temperature, and then to the solidus temperature, the solubility product of Ti and N in liquid phase exceeds the equilibrium solubility product for TiN formation. Thereafter, TiN nucleates on the oxide inclusion. With the successive decrease of liquid superalloy temperature, NbC precipitates on the pre-formed TiN. At the later stage, the process converts to the interdiffusion of carbide-forming and nitride-forming atomics, *i.e.*, Nb, Ti, C, and N, at layers interface. This is the reason that the region concentrated with Ti and N includes a small amount of Nb and C, and the Nb-concentrated and C-concentrated region contains a small amount of Ti and N. It can be seen from element mappings shown in Figure 3 that the distributions of Nb and C in Ti-concentrated and N-concentrated region are not very even, and the distributions of Ti and N in Nb-concentrated and C-concentrated region are also not very even. This should be the result of atomics diffusion. Further study is necessary to understand the thermodynamics and kinetics of the formation and evolution of carbide, nitride and carbonitrides in Inconel 718 superalloy.

The carbonitrides in the superalloy ingots (*i.e.*, ESR-1 and ESR-2) produced without calcium addition are clustered block or in single octahedral form, as shown in Figure 4. It is considered to be due to the presence of $MgO{\cdot}Al_2O_3$ spinels and MgO inclusions. When high-melting-point oxide inclusions, such as $MgO{\cdot}Al_2O_3$ and MgO inclusions, pre-exist in liquid superalloy, the nitride can precipitate on them and the carbide can then form on this nitride under small supercooling. The carbide has more time for growing and reaching its equilibrium morphology, which is octahedral shape,[28,42] than that without pre-existence of $MgO{\cdot}Al_2O_3$ and MgO inclusions. Therefore, the morphology of the carbide containing a small amount of Ti and N nucleated on high-melting-point oxide inclusion closes to or reaches its equilibrium morphology.

In the case of superalloy ingot produced with a proper amount of calcium addition in ESR process, the morphology of the observed carbonitrides in the ingot is skeleton-like shape, as shown in Figure 4(d). This might be attributed to the fact that, with proper amount of calcium addition, the oxide inclusions were changed into low-melting-point $CaO\text{-}MgO\text{-}Al_2O_3$ system inclusions around the $MgO{\cdot}Al_2O_3$ spinel core. The carbide formed on the nitride which precipitated on $CaO\text{-}MgO\text{-}Al_2O_3$ system inclusion has no sufficient time to reach or close to the equilibrium morphology (*i.e.*, octahedral form).

After excessive amount of calcium addition, CaO inclusions are mainly oxide cores for nitrides nucleation, except for a few $CaO\text{-}Al_2O_3$ system inclusions.

However, nearly all carbonitrides are still skeleton like, although CaO inclusion has high melting point. No clear difference in the morphology between the carbonitrides (Nb,Ti)CN in ESR-3 and that in ESR-4 can be observed. The reason is not clear currently.

Electroslag remelting has outstanding advantage in removing oxide inclusions. It is considered that many original inclusions in the electrode (*i.e.*, original MgO or $MgO{\cdot}Al_2O_3$ inclusions) have been removed before liquid superalloy solidification from the bottom of shallow liquid metal pool in ESR process under the present ESR experimental conditions. During the cooling of liquid metal pool, the oxygen solubility in liquid metal phase decreases with decreasing temperature. The supersaturated oxygen would react with dissolved Mg and Al in the liquid steel pool forming new oxide inclusions. It is not possible to distinguish between the original $MgO{\cdot}Al_2O_3$ spinel inclusions of the electrode remaining in ingot and newly formed $MgO{\cdot}Al_2O_3$ spinel inclusions in liquid metal pool.

IV. CONCLUSIONS

1. All the observed oxide inclusions in superalloy ingots produced under different remelting conditions were nucleation sites of outer (Nb,Ti)CN layers. Oxide inclusions in the consumable electrode are $MgO{\cdot}Al_2O_3$ spinels as dominating precipitates and some pure MgO. All the oxide inclusions in ESR ingots produced without calcium treatment in ESR process are $MgO{\cdot}Al_2O_3$ spinels. In the case of proper amount of calcium addition in ESR process, the original $MgO{\cdot}Al_2O_3$ spinels can be effectively modified to the complex oxide inclusions in the form of $MgO{\cdot}Al_2O_3$ core surrounded by $CaO\text{-}MgO\text{-}Al_2O_3$ layer in superalloy ingot. Excessive amount of calcium addition induces many CaO inclusions and formation of a few $CaO\text{-}Al_2O_3$ system inclusions in ESR ingot.
2. All carbonitrides (Nb,Ti)CN precipitated around oxide inclusion core exhibit a two-layer structure, except for those with single (Nb,Ti)CN layer containing a small amount of Ti and N in the ingot produced with proper amount of calcium addition in ESR process. For carbonitrides (Nb,Ti)CN with a two-layer structure, the outer (Nb,Ti)CN layer has a higher atomic percentage of Nb than that of Ti as well as a small amount of Ti and N. The inner (Nb,Ti)CN layer has a higher atomic percentage of Ti than that of Nb, and contains a small amount of Nb and C. The atomic ratio of Nb/Ti in different carbonitrides is relatively constant. The size of the carbonitrides in different superalloy ingots ranges from 5 μm to 15 μm.
3. Calcium treatment in ESR process has resulted in a significant change in the morphology of carbides containing a small amount of Ti and N from single octahedral form or clustered block to skeleton-like shape. The precipitation of primary carbonitrides (Nb,Ti)CN during solidification would be suppressed by reducing the oxide inclusion content through reducing oxygen content in the superalloy, which would indirectly decrease the carbonitrides (Nb,Ti)CN nucleation sites.
4. Two-dimensional examination, *i.e.*, the direct observation on well-polished surface by SEM-EDS, can hardly represent the actual size and morphology of the precipitates in ingot, but it can reveal their types.

ACKNOWLEDGMENTS

The authors would like to express their sincere thanks to Prof. Ke-ming Fang for his fruitful discussions, Prof. Juan-ling Sui of Beijing General Research Institute of Mining and Metallurgy for her help in carrying out SEM-EDS experiments. The financial support provided by the International Science and Technology Cooperation and Exchange of Special Projects (grant no. 2010DFR50590) is greatly acknowledged.

REFERENCES

1. A. Choudhury: *ISIJ Int*., 1992, vol. 32, pp. 563–74.
2. W.R. Sun, J.H. Lee, S.M. Seo, S.J. Choe, and Z.Q. Hu: *Mater. Sci. Eng. A*, 1999, vol. 271, pp. 143–49.
3. F.W. Chen, X.B. Huang, Y. Wang, Y. Zhang, and Z.Q. Hu: *Mater. Lett*., 1998, vol. 34, pp. 372–76.
4. X.C. Chen, R. Fu, H. Ren, and D. Feng: *China New Technol. Prod*., 2011, vol. 10, pp. 1–2.
5. J. Campbell and M. Tiryakioğlu: *Metall. Mater. Trans. B*, 2012, vol. 43B, pp. 902–14.
6. T. Denda, P.L. Bretz, and J.K. Tien: *Metall. Trans. A*, 1992, vol. 23A, pp. 519–26.
7. J. Chen, J.H. Lee, C.Y. Jo, S.J. Choe, and Y.T. Lee: *Mater. Sci. Eng. A*, 1998, vol. 247, pp. 113–25.
8. L. Liu, F. Sommer, and H.Z. Fu: *Scripta Metall. Mater*., 1994, vol. 30, pp. 587–91.
9. J. Chen and B.Y. Huang: *J. Mater. Sci. Technol*., 1999, vol. 15, pp. 48–52.
10. A.K.M.B. Rashid and J. Campbell: *Metall. Mater. Trans. A*, 2004, vol. 35A, pp. 2063–71.
11. P.N. Quested and M. Mclean: *Mater. Sci. Eng*., 1984, vol. 65, pp. 171–80.
12. R. Fernandez, J.C. Lecomte, and T.E. Kattamis: *Mater. Trans*., 1978, vol. 9A, pp. 1381–86.
13. C.B. Shi, X.C. Chen, H.J. Guo, Z.J. Zhu, and H. Ren: *Steel Res. Int*., 2012, vol. 83, pp. 472–86.
14. X. Cao and J. Campbell: *Metall. Mater. Trans. A*, 2003, vol. 34A, pp. 1409–20.
15. X. Cao and J. Campbell: *Metall. Mater. Trans. A*, 2004, vol. 35A, pp. 1425–35.
16. K. Liu, X. Cao, and X.-G. Chen: *Metall. Mater. Trans. A*, 2011, vol. 42A, pp. 2004–16.
17. J.I. Takamura and S. Mizoguchi: *Proc. 6th Int. Iron Steel Cong.,* ISIJ, Tokyo, Japan, 1990, p. 591.
18. E.B. Pretorius, H.G. Oltmann, and T. Cash: *Iron Steel Technol*., 2010, vol. 7, pp. 31–44.
19. N. Verma, M. Lind, P.C. Pistorius, R.J. Fruehan, and M. Potter: *Iron Steel Technol*., 2010, vol. 7, pp. 189–97.
20. Y.J. Kang, F. Li, K. Morita, and D. Sichen: *Steel Res. Int*., 2006, vol. 77, pp. 785–92.
21. H. Yafang and M.C. Chaturvedi: *J. Mater. Sci. Technol*., 1989, vol. 5, pp. 79–84.
22. T. Antonsson and H. Fredriksson: *Metall. Mater. Trans. B*, 2005, vol. 36B, pp. 85–96.
23. G.A. Rao, M. Kumar, M. Srinivas, and D.S. Sarma: *Mater. Sci. Eng. A*, 2003, vol. 355A, pp. 114–25.
24. F.C. Liu, X. Lin, C.P. Huang, M.H. Song, G.L. Yang, J. Chen, and W.D. Huang: *J. Alloys Compd*., 2011, vol. 509, pp. 4505–09.
25. X.C. Chen, R. Fu, and H. Ren: Chinese Patent, 201110084387.X, 2011.

26. J.H. Wei and A. Mitchell: *Acta Metall. Sin.*, 1984, vol. 20, pp. B261–79.
27. T. Antonsson and H. Fredriksson: *Metall. Mater. Trans. B*, 2005, vol. 36B, pp. 85–96.
28. Z.B. Li: *Electroslag Metallurgy Theory and Practice*, Metallurgical Industry Press, Beijing, China, 2010.
29. A.H. Dilawari and J. Szekely: *Metall. Trans. B*, 1978, vol. 9B, pp. 77–87.
30. Q.Y. Huang, S.J. Zhang, and B.L. Zhen: *Iron Steel*, 1981, vol. 16, pp. 41–47.
31. L. Lin and H.Z. Fu: *Mater. Sci. Progr.*, 1989, vol. 3, pp. 396–400.
32. X.B. Huang, Y. Zhang, Y.L. Liu, and Z.Q. Hu: *Metall. Mater. Trans. A*, 1997, vol. 28A, pp. 2143–47.
33. A. Mitchell and T. Wang: *Superalloys 718, 625, 706 and Various Derivatives*. Ed. A.E. Loria, TMS, Warrendale, PA, 2001.
34. L. Liu, B.L. Zhen, A. Banerji, W. Reif, and F. Sommer: *Scripta Metall. Mater.*, 1994, vol. 30, pp. 593–98.
35. S.W. Cho and H. Suito: *ISIJ Int.*, 1994, vol. 34, pp. 746–54.
36. H. Ohta and H. Suito: *ISIJ Int.*, 2003, vol. 43, pp. 1293–300.
37. A. Karasev and H. Suito: *Metall. Mater. Trans. B*, 1999, vol. 30B, pp. 249–57.
38. E.T. Turkdogan: *Physical Chemistry of High Temperature Technology*, Academic Press Inc., New York, NY, 1980.
39. K. Fujii, T. Nagasaka, and M. Hino: *ISIJ Int.*, 2000, vol. 40, pp. 1059–66.
40. J.H. Park and H. Todoroki: *ISIJ Int.*, 2010, vol. 50, pp. 1333–46.
41. M. Jiang, X.H. Wang, B. Chen, and W.J. Wang: *ISIJ Int.*, 2010, vol. 50, pp. 95–104.
42. L. Liu, H.Z. Fu, and Z.X. Shi: *Acta Metall. Sin.*, 1989, vol. 25, pp. A282–87.